Theoretical Prediction and Experimental Verification of the Unbalanced Magnetic Force in Air Bearing Motor Spindles

Quanhui Wu[1], Yazhou Sun[1*], Wanqun Chen[1] , Qing Wang[2] and Guoda Chen[3]

[1]School of Mechatronics Engineering, Harbin Institute of Technology, Harbin 150001, P. R. China

[2]Department of Engineering, Durham University, Durham DH1 3LE, United Kingdom

[3]Key Laboratory of E&M, Ministry of Education & Zhejiang Province, Zhejiang University of Technology, Hangzhou 310032, P. R. China

Abstract

Dynamic vibrations of air bearing motor spindles have significant influence on the surface quality in ultra-precision machining. In this article, the influence of the vibration caused by the unbalanced magnetic force on the diamond turning is investigated on the basis of the theoretical and experimental method. A permanent magnet motor model (10 poles and 12 slots) is built and then simulated to gain a periodic unbalanced magnetic force. The effects of unbalanced magnetic force on the inclination of the spindle shaft is analyzed, which would affect the surface quality of the workpiece, and the surface topography of the work piece is predicted during an unbalanced magnetic force acting on air bearing motor spindle. The theoretical analysis and experimental turning results validate that the angle between the direction of unbalanced magnetic force and the feed direction has a certain relationship with the profile of the machined surface. Also, under different turning speeds and directions, the surface topography of the machined workpiece shows a 10-cycle per-revolution pattern, which has good agreement with the simulations of periodic unbalanced magnetic force. This research work provides a theoretical foundation for the fault diagnosis of air bearing motor spindle caused by motor rotor eccentricity and its effect on surface generation in turning.

Keywords

Air Bearing Motor Spindles, eccentricity, unbalanced magnetic force, vibration, prediction, machining verification

Introduction

Ultra-precision diamond turning is widely used in manufacturing optical surfaces, and ultra-precision machine tools are irreplaceable to meet the strict requirements for precision machining. The overwhelming majority of ultra-precision machine tools are equipped with Air Bearing Motor Spindles (ABMS), which is the core component of ultra-precision machine tools for achieving the desired accuracy and roughness of workpieces surface[1-3]. Figure 1 illustrates the schematic diagram of an ABMS, which is supported by two axial aerostatic bearings and a journal bearing, and the spindle shaft and the motor rotor are connected directly. Because ABMS is a complex system, the manufacturing imperfections and assembly misalignments affect the rotation accuracy of ABMS, which introduces unwanted motion errors to the rotational spindle system such as radial, axial, or tilt

Abbe offset errors,[4,5] . Those errors in ABMS affect the machining productivity and quality of the workpiece surface. Therefore, many scholars have studied the dynamic properties of ABMS, [6-8] and they have also made many achievements in the spindle system. Indeed, there are still many problems with the spindle system, which need to be studied deeply, and these problems also have a great effect on the machining performance, which could obviously reduce machining accuracy.

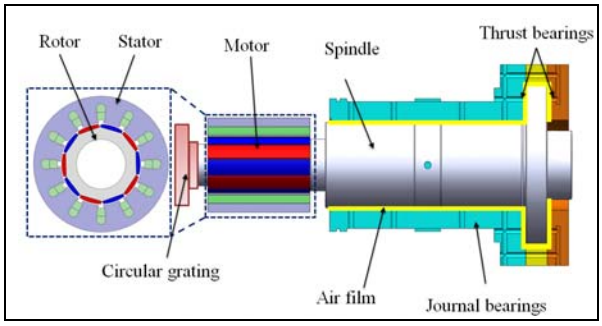

Figure 1. Schematic view of an ABMS.

ABMS is uaually driven by a permanent magnet synchronous motor (PMSM), so the motor also has a great effect on the performance of ABMS. According to different power supplies, motors can be categorized as a DC motor or an AC motor, such as in a brush-less permanent magnet synchronous motor (BLPMSM), AC brush-less induction asynchronous motor (BLIAM). In addition, a motor that generates a square wave or a trapezoidal wave is a brushless direct current motor (BLDCM), and a motor that generates a sine wave is a permanent magnetic synchronous machine (PMSM). By changing the rotating magnetic field of the stator, the rotor in BLIAM generates the induced current and produces electromagnetic torque. The motor rotor cannot produce a magnetic field directly, so the rotor rotating speed is less than the synchronous speed. Besides, compared with BLIAM, BLPMSMs have obvious advantages, such as high power density, high efficiency, high reliability, small size and better dynamic performance.[9]

Ideally, the motor rotor center is concentric with the motor stator center, and the electromagnetic force acting upon the rotor surface is balanced.[10] However, due to tolerance in manufacture or assembly, motor rotor eccentricity (MRE) between stator axis and rotor axis is unavoidable in practice.[11] If the motor rotor axis is misaligned with the center axis of the stator bore, the air-gap magnetic field becomes distorted, resulting in an Unbalanced Magnetic Force (UMF). Unfortunately, UMF could degrade motor performance and increase vibrations and acoustic noise. To reduce magnetically induced vibrations and noise, Song et al.[12] investigated the relative amplitudes of the harmonics of UMF generated by the MRE. Han et al.[13] proposed a magnetic equivalent circuit modeling method to calculate both the radial and the tangential eccentric force of motors. To control motor vibration and improve the performance, Qiao et al. [14] proposed and active control scheme with built-in force actuator for unbalanced vibration of the flexible motorized spindle and applied an unbalance identification algorithm to control the tool vibration. Wang et al.[15] studied the frequency spectrum characteristics of electromagnetic force under different rotor eccentricities to suppress electromagnetic vibrations. Admittedly, motor experts have analyzed many working properties of motors,[16] but few studies have been carried out to analyze the motor effects of ABMS on the actual processing. Because ABMS is the integration of a PMSM and air bearings, ABMS has the complexity of multiphysics coupling characteristics,[17] and mechanisms of ABMS have

changed considerably in comparison with the traditional electromechanical drive system.

At present, a series of researches on dynamic performance of ABMS has been discussed, both theoretically and experimentally. For example, Zhang et al. [18] built up a dynamic spindle model to describe its dynamic responses, involving translational motions and tilting motions. Liang et al.[19] designed and optimized the structure of an ultra-precision spindle for crystal machining. Chen et al. [20,21] pointed to the fact that the measurement and analysis of ABMS had great significance for deeply understanding the spindle performance and improving machining quality. Hence, many new concepts of ABMS have been provided, and also new approaches have been developed for implementing ABMS.[1,22, 23] However, some key technical problems are still not solved. In the past, the mechanical characteristics of the spindle shaft and the electrical characteristics of the motor were separately analyzed in ABMS. Nevertheless, because a motor rotor and spindle shaft are coupled as a body, they always interact with each other, so the spindle system shows a multi-field and multi-parameter coupling relationship.[24]

A common source of noise and vibrations in a PMSM is the UMF due to MRE.[25,26] Motor experts study UMF which generates periodic fluctuations caused by MRE. Ma et al.[27] studied UMF when there is MRE in PMSM; investigated the influence of slot-pole combination on UMF in PMSM having different MRE and magnetizations, which shows the motors with different magnetizations have different UMF due to MRE as magnet thickness and slot-pole combination vary; and also analyzed the radial vibration forces in 10-pole/12-slot motors.[28] In addition, in order to analyze the influence of UMF on the axial vibration forces in 10-pole/12-slot motors.[28] In addition, in order to analyze the influence of UMF on the axial vibration of the spindle system, Usman[29] analyzed the effects of a motor on the hydrostatic bearing system by installing an axial displacement ball target. The tested signals showed that the spindle shaft produced a nine-cycle-pr-revolution pattern in the axial error signal, which was consistent with the motor poles when the spindle rotates at different speeds (500-3000r/min). Meanwhile, in order to further study the effects of motor characteristics on machining surface deeply, Zhang et al.[30] discussed the dynamic characteristics of spindle imbalance-induced forced vibration and its effect on surface generation in diamond turning, which adopted a 12-pole permanent magnet motor as the driving source of an ultra-precision spindle system. Under the action of UMF on the motor rotor, the spindle vibration with a fundamental cyclic frequency of $2p$ per revolution (the spindle motor pole number) would occur to produce the corresponding straight radial patterns at the machined surface. Besides, previous work has done some research on MRE of a vertical ultra-precision spindle,[31] and a range of rotor eccentricities was calculated to assess the impact of UMF on the spindle performance. MRE has a significant influence on the spindle vibration indeed, which dramatically reduces the surface quality.

In the field of ultra-precision machining, the machining errors, especially geometric errors, have a significant influence on the form accuracy of mechanical surfaces. Lots of researchers have been done on the surface roughness error or figure error in turning,[32] and a systematic review of influencing factors and theoretical modelling methods of surface roughness in turning process has been presented.[33]

However, some surface topography problems of end face turning have not been studied in depth, so it is a very effective method to study in turning problem using end face prediction. Surface generation simulations can be used to design machine tools, which briage the gap between the machine tool performance and the surface topography generation.[34] Therefore, in order to study the influence of the motor vibration problems on the turning, it is a useful method to study motor vibrations in ABMS though the surface topography simulation.

In order to study deeply the dynamic characteristics of the motor on horizontal ABMS and MRE on the diamond turning, an ABMS is used as the research object in this study, which adopts a motor (10 poles and 12 slots) as the driving source. The characteristics of UMF are presented and its effects on ABMS are discussed. The Finite Element Method (FEM) is used to analyze the MRE, and the dynamic behaviors of ABMS caused by UMF are presented. In addition, a numerical surface simulation model is established to investigate the influence of MRE on the turning work-piece surface topography. The workpiece surface, which shows a concave or convex shape for different turning directions, is further explained. Furthermore, under different turning speeds and directions, a 10 cycle per revolution pattern is predicted for the machined surface, on the basis of the proposed surface simulation model. Experimental turning results are conducted to validate the theoretical analysis.

UMF Induced by Rotor Eccentricity

Maxwell Stress Tensor

In a PMSM, the main component of the magnetic forces acting on the motor rotor perimeter is the tangential direction force to drive the rotor rotating. Because of the manufacturing tolerances, the rotor axis is not concentric with the stator axis, and there will be an UMF acting on the rotor and stator. An approach for calculating UMF is to derive the components of the magnetic force from the magnetic field. In the air gap of PMSM, the radial and tangential delta components of force densities can be evaluated using the Maxwell stress method. As the magnets in the rotor have a much higher permeability than air, the tangential delta component of air-gap flux density is much smaller than the radial component, so the tangential delta flux density can be negligible. The magnetic force is generally expressed as [35,36]

$$f_r = (B_r^2 - B_\theta^2)/(2\mu_0) \approx B_r^2/(2\mu_0) \quad (1)$$

$$f_\theta = (B_r B_\theta)/\mu_0 \quad (2)$$

Where f_r denotes the radial force density, f_θ denotes the tangential force density, B_r and B_θ denote the radial and tangential circumferential air-gap flux density, respectively. μ_0 denotes the permeability of air, and θ denotes the angular position of the rotor with reference to the axis of a magnetic pole.

UMF acting on the perimeter of the motor rotor can be obtained as the integral of the radial force density along the rotor perimeter, which is expressed as

$$F = \int_0^{2\pi} f_r \cdot r d\theta \quad (3)$$

Using the Cartesian coordinate system, the radial force density is converted to the corresponding electromagnetic force density, which can be expressed as

$$f_x = f_r \cos\theta \quad (4)$$

$$f_y = f_r \sin\theta \tag{5}$$

Thus, the UMF acting on the rotor can be obtained by integrating the unbalanced magnetic tension on the corresponding rotor surface, which can be expressed as

$$F_x = \int_0^{2\pi} f_x \cdot r d\theta \tag{6}$$

$$F_y = \int_0^{2\pi} f_y \cdot r d\theta \tag{7}$$

Therefore, the total electromagnetic force of the motor can be calculated as

$$F = \sqrt{F_x^2 + F_y^2} \tag{8}$$

UMF under MRE

In an ideal PMSM, the rotor center is aligned with the center of the stator bore, and the rotor center of rotation is at the same position as the geometric center of the stator bore, as shown in Figure 2 (a). However, in reality, the rotor center is not concentric with the stator bore, which commonly consists of two forms: static style or dynamic style. Usually, the static eccentricity and the dynamic eccentricity are simultaneously present in the motor.[37,38] In the case of a static eccentricity, the air gap between the rotor and the sattor is stationary, and the position of the minimum radial air-gap length is fixed in a space, which is caused by the stator core ovality or incorrect rotor position, as shown in Figure 2 (b). In addition, the position of static eccentricity does not change if the rotor assembly stiffness is hard enough. A dynamic eccentricity occurs when the center of the rotor is not at the center of rotation and the minimum air gap revolves with the rotor, and the rotor rotates on the stator bore center but not on its own axis. This is a function of space and time, as shown Figure 2(c). Due to the presence of MRE, the distribution of the electromagnetic forces on the unit area between stator and rotor is not uniform. The static eccentricity tends to produce a steady pull in one direction, while the dynamic eccentricity creates a UMF vector rotating in synchronism with the rotor.

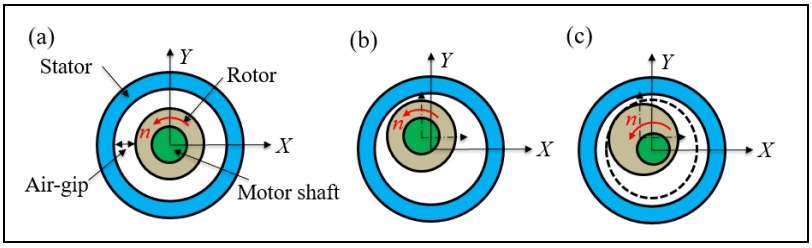

Figure 2. (a) Ideal motor (No eccentricity); (b) Static eccentricity; (c) Dynamic eccentricity.

According to the Maxwell stress tensor method and FEM, the radial and the tangential magnetic traction acting on the rotor can be calculated. In general, the magnetic force caused by the varying air-gap electromagnetic fields can be decomposed into a delta tangential force and an UMF on the rotor. The delta tangential force is smaller than UMF, thus it is neglected here. In order to clearly describe the motor rotor and the air gap, the sizes and positions of the rotor and stator are plotted with exaggeration. The UMF F distribution is shown as Figure 3, which shows a schematic of the

geometry of a permanent magnet motor with MRE. In this figure, n represents the rotating speed, and points O and o represent the centers of the rotor and stator, respectively. The stator and the rotor axes are assumed to be parallel; e represents the eccentricity between points O and o; o-xy represents the coordinate system of the rotor, which uses the center o as the origin, x and y represent the lateral coordinates of the rotor center, and O-XY represents the coordinate system of the stator.

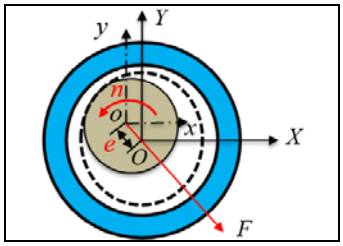

Figure 3. Cross section of motor with MRE.

In an ABMS, the spindle shaft is driven by an overhang motor. In this type of structure, there are some geometric errors between stator and rotor caused by the manufacturing or assembly process, which contains the static eccentricity and dynamic eccentricity. In addition, because a fixed clamp for the workpieces is fixed at the end of the aerostatic bearing in the machining process, the spindle system that has been balanced becomes a new imbalance system. The stator and the rotor axes are not parallel, resulting in the variation of flux path and equivalent air-gap length. As seen in Figure 4, there is a non-coincidence in the axis between the stator and the motor rotor, which is a tilting angle between the two axes. The rotor core is tilted with an angle γ on the rotor shaft leading to a non-uniform electromagnetic force over the core length，so that the UMF F produces three components: the static UMF, dynamic UMF and incline UMF. Moreover, the UMF can decompose in three directions, which is the radial x, y and axial z directions.[39] In addition, the inclination angle γ is relatively small. The UMF F can be calculated according to the eccentricity between the stator and rotor, without tilt angle. The axial component force F_0 is calculated as Eq. (9).

$$F_0 = F\sin\gamma \tag{9}$$

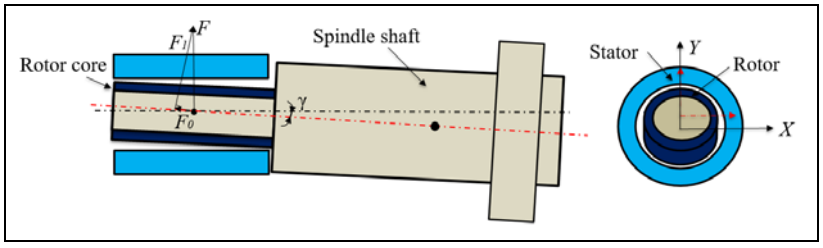

Figure 4. Tilt of the rotor core.

UMF calculation

UMF is difficult to calculate using a single analytical method. Based on the electromagnetic theory of the motor, FEM is useful for calculating the UMF, which considers the impacts of the saturation factor and current waveform. Meanwhile, FEM can provide an accurate calculation for the dynamic motor responses when a motor is subjected to UMF. The software of Ansoft Maxwell specifically emulates motor characteristics, which is a FEM based on motor design principles, so it can be used to accurately

simulate the motor model.[40]

To study the effect of UMF on the motor rotor, a model of a 10/12 motor is simulated, and Table 1 lists the detailed parameters of the motor.

Table 1. Parameters of spindle motor

Parameters	Rotor	Stator
Outer diameter(mm)	64	110
Inner diameter(mm)	50	66
Poles/ slots	10/12	
Total length(mm)	110	
Rated angular velocity(rpm)	1000	
Rated power(kW)	4	
Air-gap(mm)	1	
Winding form	3-phase of double layer windings	

To simplify the motor model and increase calculation efficiency, the permeability between stator and rotor is assumed to be infinite. The rotor inner circle and the stator outer circle are selected as the boundary, which has no magnetic leakage. The motor models are simulated under no-load and load conditions respectively, and are operated at the same rated speed of 1000r/min. At load conditions, the motor windings have a rated current of 6A and 3 phases. The motor models are respectively simulated at no eccentricity and eccentricity (e=5μm, the air-gap length is set to 1mm). In the case of load, Figure.5 shows the electromagnetic density cloud diagram of the motor in the non-eccentric and eccentric cases. In the same conditions (speed, position and load), when the motor has no eccentricity, the maximum electromagnetic density is 1.3503T, and the simulation of the electromagnetic cloud can be seen in Figure 5(a). When the eccentricity is set to 5μm, the maximum electromagnetic density is 1.7045T, which can be seen in Figure 5(b). Therefore, in the eccentric case, the electromagnetic density becomes larger, and the eccentric case is more likely to produce magnetic saturation.

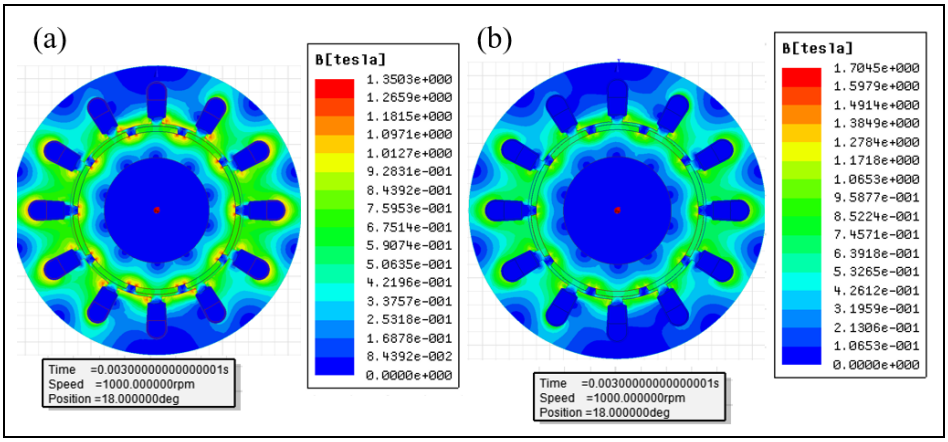

Figure 5. Electromagnetic cloud in the case of load:(a)No eccentricity; (b)Eccentricity (*e*=5μm).

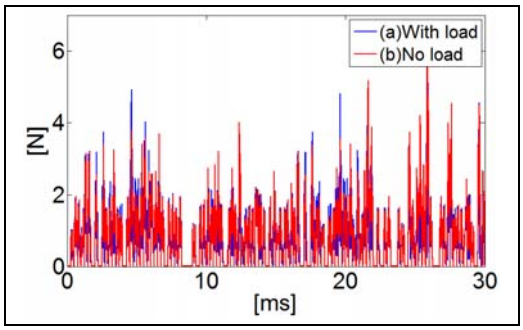

Figure 6. UMF curve of motor rotor (No MRE).

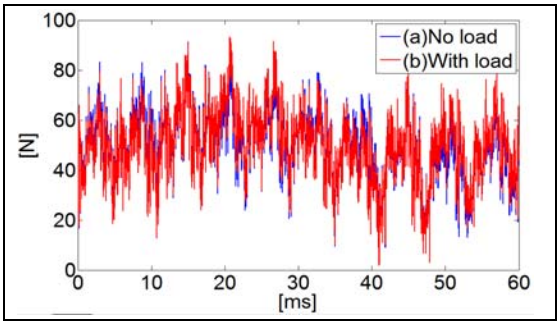

Figure 7. UMF curve of motor rotor (MRE, *e*=5μm).

Figure 6 describes UMF with no eccentricity, Figure 6(a) represents UMF with a no-load condition, and Figure 6(b) represents UMF with a load condition. It can be seen from Figure.6 that UMF values are very small, almost all less than 6N. However, in the case of MRE, the UMF values become large. As shown on Figures 7(a) and (b), the UMF values of the motor rotor are slightly different in the cases of no-load and load conditions, having the same ripples of 10 peaks in one cycle，and the average values become greater than 40N.

Electromagnetic effects on ABMS in Z axis

Turning path offset

ABMS is an ultra-precision spndle system, and the schematic diagram of the supporting form of ABMS is shown in Figure 8. Under normal conditions, the periodic UMF points to the direction of the smallest air gap, which always points to the center axis of the rotor and actually tilts the shaft in the air bearing. The dotted line of the spindle in Figure 8 indicates that spindle shaft is subjected to the UMF, and the solid line structure indicates the initial position of the spindle shaft. It can be noted that the spindle periodically swings around its centroid *M*.

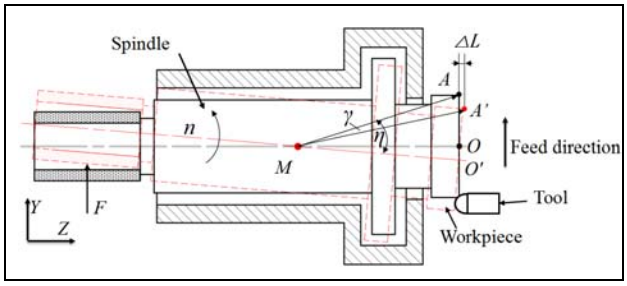

Figure 8. Spindle shaft tilt caused by UMF.

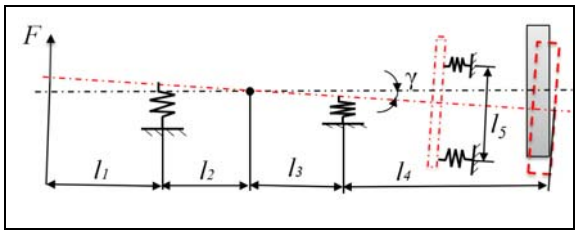

Figure 9. Sample model of the spindle shaft tilt.

Under the action of UMF, the spindle system produces tilt. The inclination angle between the actual position of the spindle axis and ideal axis position is γ, which is shown in Figure 9. In this figure, l_1=127 mm denotes a distance between the position of UMF (selecting the midpoint of the motor's axial length) to the air inlet position of the left radial support, l_2+l_3=130 mm denotes the distance between two rows of radial air inlets, l_4=225 mm denotes the distance between the positions of the

right radial air inlet and the workpiece surface; and l_5=156 mm denotes the diameter of the axial air inlets. In addition, the spindle system is designed to have a journal stiffness of 350 N/μm, an axial stiffness of 300N/μm. The mass of the spindle system is 28 Kg, and the inertia of the spindle system moment is 0.045 Kg.m^2. According to the simulation of Figure 7, the stable component of UMF is assumed as F_1=50N, the amplitude of vibration of UMF is 15N, and the tilting angle γ produced by the spindle is 1', resulting in a slope of k = tan1'. As seen from Figure 8 and 9, the Z axial displacement can be calculated using equations (10) and (11). Therefore, the amplitude ΔL on the workpiece surface is affected by the spindle tilt angle and the turning position. In addition, the slope k of the workpiece surface caused by the inclination of the spindle axis can be expressed as equation (12).

$$\Delta L = R\cos(\eta - \gamma) - R\cos\eta \tag{10}$$

$$R = \sqrt{(l_3 + l_4)^2 + r^2} \tag{11}$$

$$k = \tan\gamma \tag{12}$$

Where R denotes the distance (MA) between the centroid M and the machining point A, η denotes the angle between the line (MA') and the vertical direction, γ denotes the torsion angle formed by the line (MA) and the line (MA'), and r denotes the distance between the machining point and the workpiece center O'.

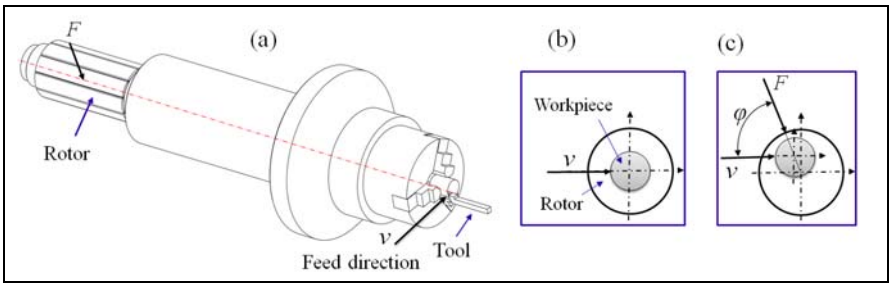

Figure 10. (a)Machining diagram of ABMS; (b) Turning with no MRE; (c) Turning with MRE.

The machining process diagram of ABMS is shown in Figure 10. The case of no eccentricity is shown in Figure 10(a), and the center projection of the workpiece and the motor rotor is in the coincidence position. However, due to presence of UMF, the spindle is tilted, so the center projection of the workpiece and the motor rotor changes the position, as shown as Figure 10(b). The center of the workpiece is eccentric toward the opposite direction of UMF, where φ is the angle between the feed direction and the UMF F direction. If the angle φ is an acute angle, k is a positive value. In the opposite case, if the angle φ is an obtuse angle, k is a negative value.

Simulation of surface topography

Surface quality has been recently recognized as an indispensable functional element for detecting workpieces,[41] so there is a need for an understanding of the properties resulting from topography. To clearly explain the effects of UMF on a workpiece surface, a surface topography model is built, which is obtained using MATLAB simulation. Combined with the effect of UMF on the Z axial displacement of ABMS vibration, the tool path on the workpiece surface can be taken as the research object. In the ideal case, the tool trajectory on the workpiece

surface is an Archimedes spiral. Nevertheless, due to UMF, the tool trajectory will change, which reflects on the workpiece surface for the *Z*-direction vibration. In order to simulate the surface topography, the rotational speed of the spindle system is set to *n*, the feed rate of the feed system is set to *f*, the vibration frequency of spindle axial drift is set to ω (related to the fluctuation frequency of UMF), the amplitude of the vibration is set to ΔL, the turning time is set to *t*, and the inclination slope of ABMS is set to *k*. According to the above parameters, the mathematical formula of surface topography can be simulated as

$$\begin{cases} x = (n \cdot f \cdot t/60) \cdot \cos(2\pi \cdot n \cdot t/60) \\ y = (n \cdot f \cdot t/60) \cdot \sin(2\pi \cdot n \cdot t/60) \\ z = \Delta L \cdot \sin(\omega \cdot \pi \cdot t) + k \cdot t \end{cases} \quad (13)$$

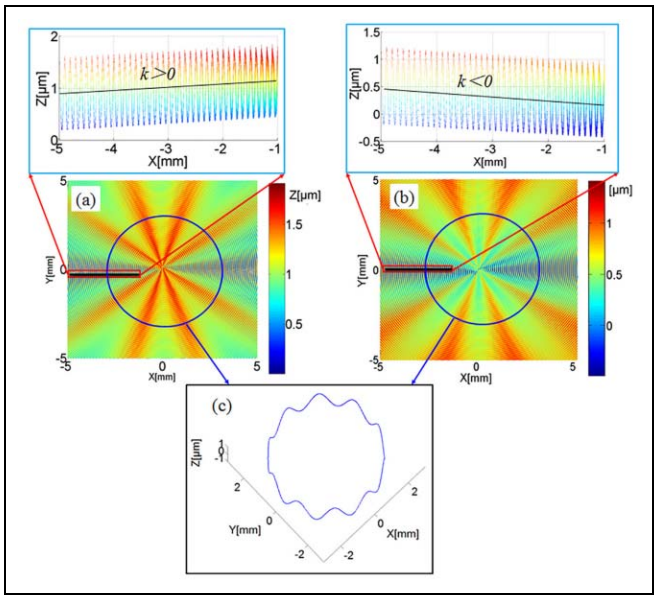

Figure 11. Surface topography of the simulation:(a) Groove shape；(b) Convex shape, (c) an extracted circle curve

Assume that the speed rotation is set to n=1000r/min, the tooltip arc radius is set to R = 1.5mm, the feed rate is set to F = 4Mm/rev, and the cutting depth is *ap*= 0.8 μm. According to the equation (13), the coefficient *k* affects the profile of the machined workpiece surface. If $k > 0$, the workpiece surface is simulated and the is shown in Figure 11(a), which shoes a convex profile in the center. In the case of $y = 0$, a surface topography is intercepted to obtain the curve of Figure 11(a). The slope *k* of the curve is a positive number, and the curve has fluctuating traces left by the tool tip. Meanwhile, in a similar phenomenon to Figure 11(a), if $k < 0$, the simulation result of the workpiece surface is shown in Figure 11(b), which shows concave in the center. The slope *k* of the curve is a negative number, and the curve also has fluctuating traces. A circle curve with a radius of 2.5 mm in the surface topography is extracted, and the extracted curve is shown in Figure 11(c); it can be seen that the simulated surface topography shows periodic ripples in the circumferential direction.

Experimental setup

In order to assess the performance of MRE on ABMS, it is necessary to carry out the corresponding experiments. Hence, a homemade ultra-precision

turning machine tool is developed, which is used to obtain the ultra-precision optical components. The ultra-precision spindle of the machine tool is selected to study UMF characteristics. The structure of the ultra-precision machine tool is shown in Figure 12, which shows the major components of the machine, including the ABMS and *X/Z* feed systems. To ensure

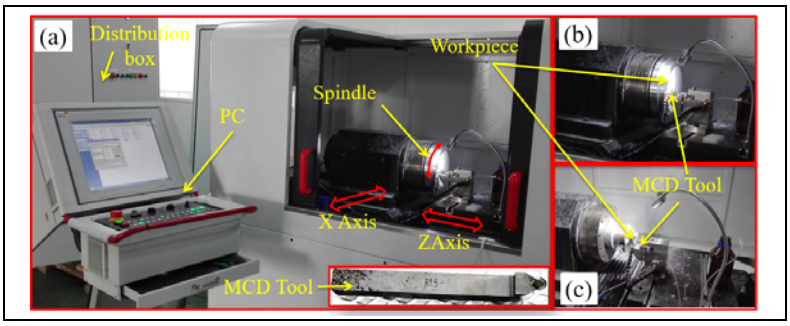

Figure 12. Ultra-precision machining tool and turning process: (a) structural layout, (b) workpiece fixed on a vacuum chuck, (c) workpiece fixed on a three-jaw chuck.

the reliability of the experimental process, the performance parameters of the machine tool are tested, shown in Figure 13. The straightness of the feed system is measured by a digital Autocollimator called Collapex AC (AcroBeam Co., Ltd, China). The tested results show that the straightness of the X/Z feed systems are better than 0.1μm/100mm, respectively. An inductive micrometer of the CERTO series (measuring range 25mm, Accuracy 0.1μm; Heidenhain Germany) is used to test the stiffness of the spindle system. The spindle rotation accuracy is better than 0.08μm. Through multiple tests, the radial stiffness of the spindle system is better than 600 N/μm, and the axial stiffness is better than 450 N/μm.

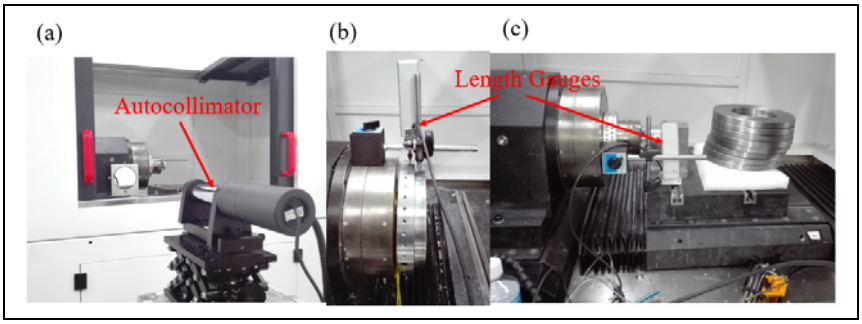

Figure 13. Testing of performance parameters: (a) Straightness test by Autocollimator; (b) Stiffness test of the spindle system;(c) Stiffness of the slide.

This ABMS is installed with a 10-pole/12-slot motor as the driving power and is equipped with an aerostatic bearing as the spindle support. The machining experiments are then carried out. The material of the turning tool is Monocrystal Diamond (MCD), the radius of the tool is 1.5mm, and the edge

radius of the tool is less than 0.3μm, as can be seen in Figure 12. In addition, the turning parameters are set as follows: the spindle speed is set to 800, 900, 1000, and 1200r/min, respectively, and the cut depth is 8μm. Two types of workpiece materials are used, the smaller size of workpiece is Al 6061 and the larger size is 5A06. The experimental results of the workpiece surface are examined by a three-dimensional (3D) rough surface tester, Phase Cam 6000 (4Sight™ interferometer, 4D Technology Corporation, USA), and the laser test wavelength is 632.8nm. the rough surface tester can detect a square range with a side length of 9mmx9mm and 2nm vertical resolution. The measurement results with only tip, tilt, and piston have been removed.

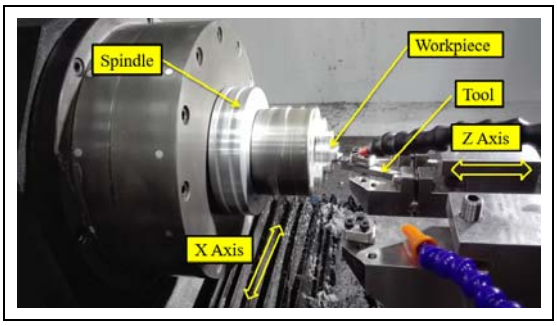

Figure 14. Turning the end face of a workpiece.

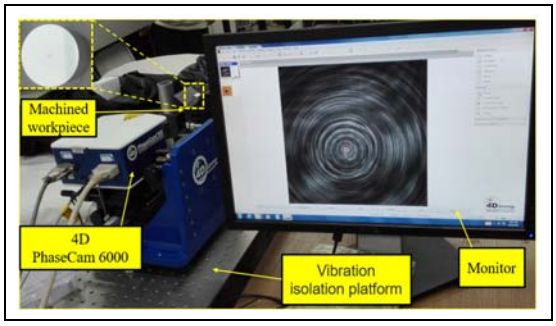

Figure 15. Testing the machined workpiece surface.

Figure 14 depicts the turning process, Figure 15 describes the testing process of the machined workpiece surface, and Figure 16 shows the different directions of the spindle rotation and feed directions of the feed system for turning.

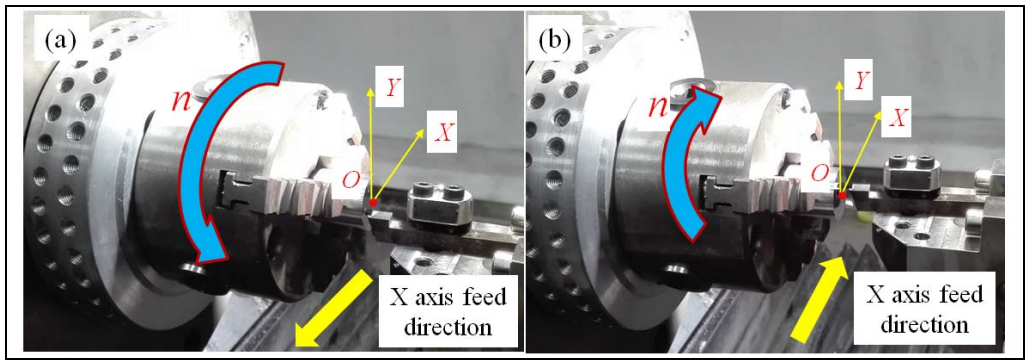

Figure 16. Turning in different turning directions:(a) Forward turning;(b) Reverse turning.

Results and discussion

First, the turning speed of the spindle is set to *n*=800r/min, the feed speed of the X axis feed system is set to 10μm/ rev. The machined workpiece is tested. The surface topographies are shown in Figure 17 and 18. The surfaces have a uniform distribution of 10 periodic ripples, which can be seen from Figure 17. The surface quality of the work piece is linearly detected, and a line is drawn from the extension to the center on the test surface topography. The position of the detected line segment is shown in Figure 18(a) and the detection result of the line segment is shown in Figure 18(b). From the test results, it can be seen that the curve value from edge to center is almost linearly reduced, the slope of the line segment is negative, and a concave profile is shown in the workpiece center.

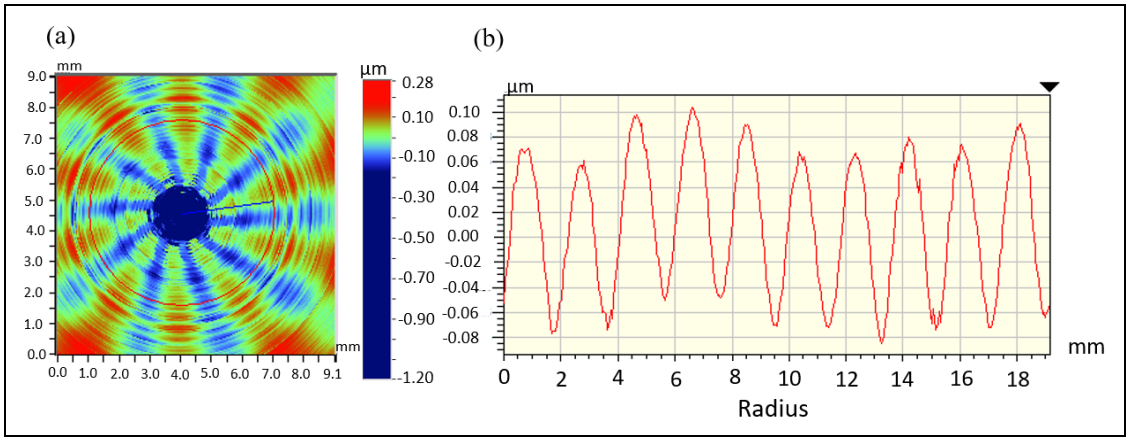

Figure 17. Test result of a circle on the machined surface (n=800r/min): (A) Position of an extracted circle curve, (b) value change of the curve.

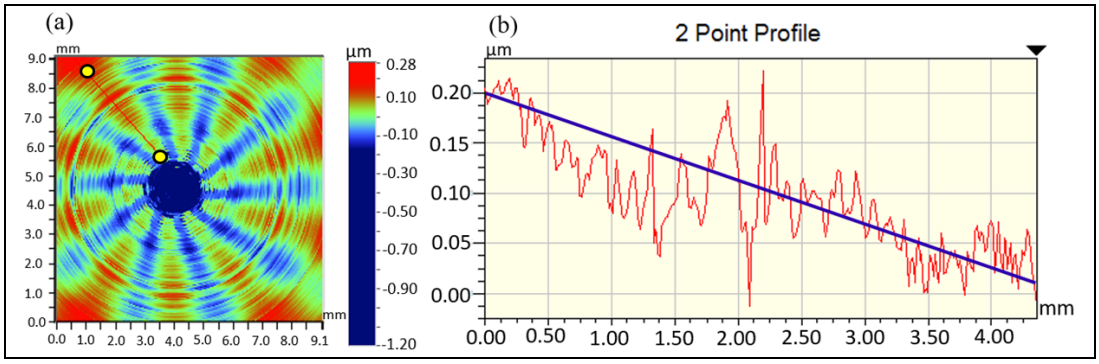

Figure 18. Test result of a line segment on the machined surface (n=800r/min): (a) position of a line, (b) value change of the curve

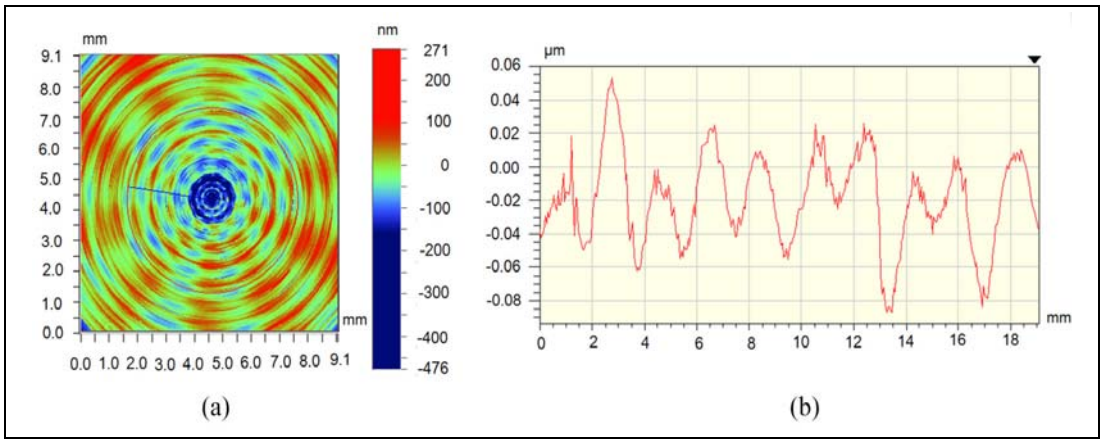

Figure 19. Tested result of a circle on the machined surface under forward turning (n=1000r/min): (a) position of an extracted circle curve, (b) value change of the curve.

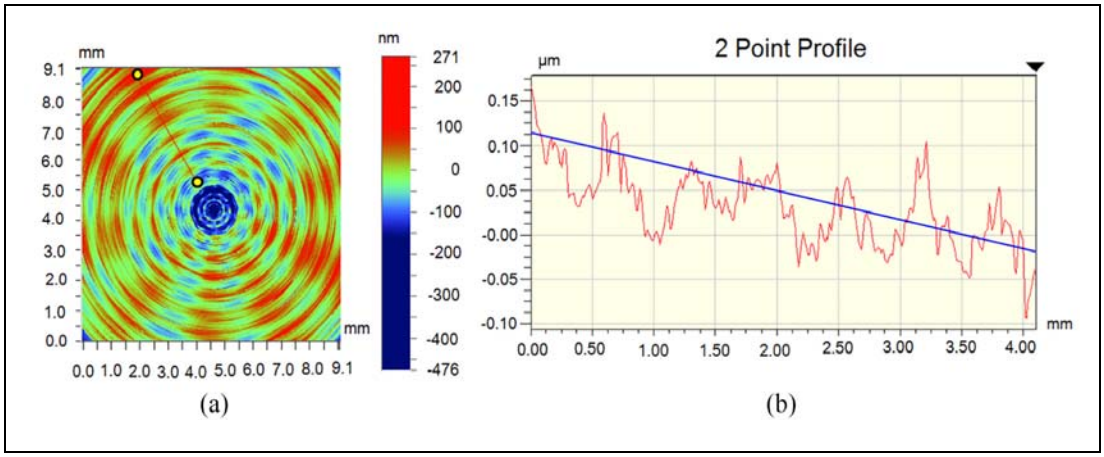

Figure 20. Tested result of a line segment on the machined surface under forward turning (*n*=1000r/min): (a) position of a line, (b) value change of the curve.

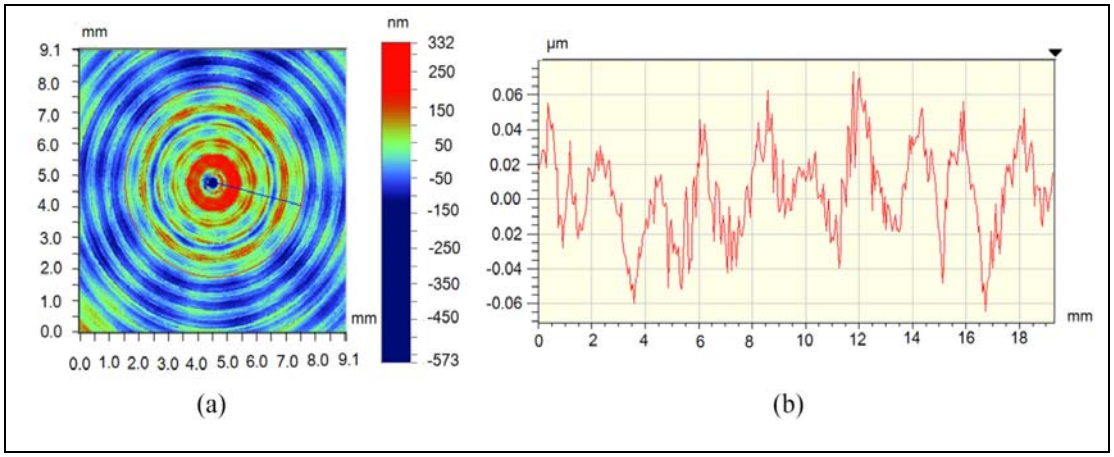

Figure 21. Tested result of a circle on the machined surface under reverse turning (*n*=1000r/min): (a) position of an extracted circle curve, (b) value change of the curve.

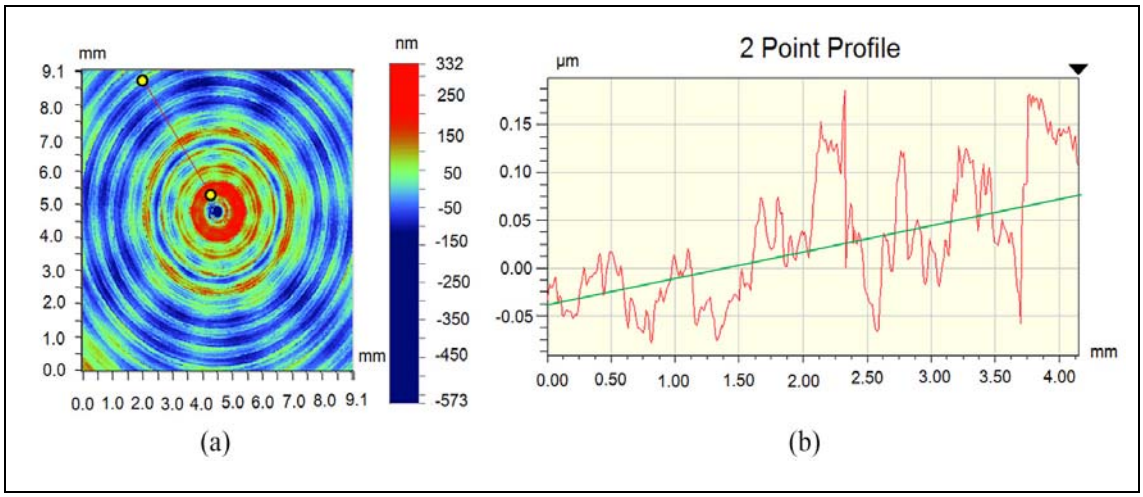

Figure 22. Tested result of a line segment on the machined surface under forward turning (*n*=1000r/min): (a) position of a line, (b) value change of the curve.

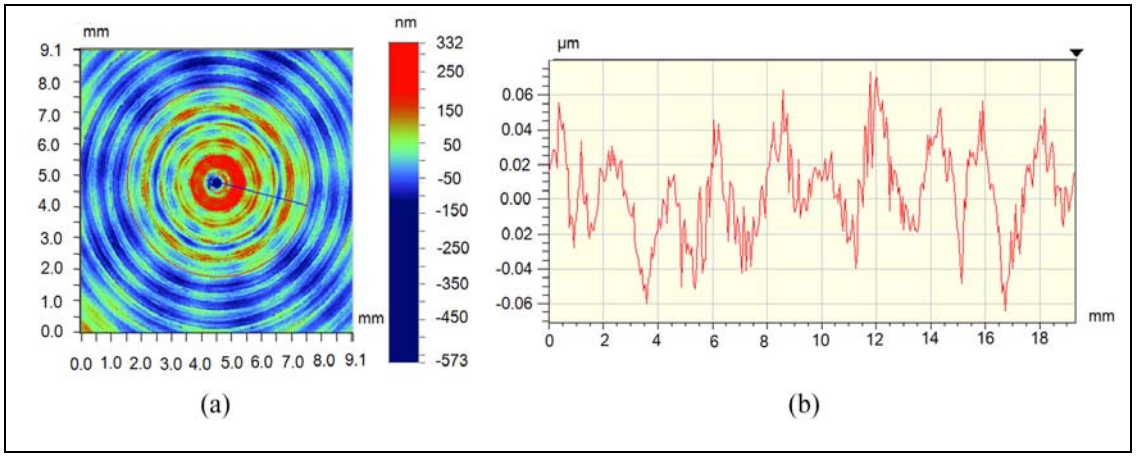

Figure 23. Tested result of a line segment on the machined surface (*n*=900r/min): (a) position of an extracted circle curve, (b) value change of the curve.

The turning speed is set to n= 1000r / min, and the feed speed for the X feed system is set to 4 μm/rev; the turning process is shown in Figure 16(a), which adopts forward turning. The tested surface topographies are shown in Figure 19 and 20. The workpiece surfaces also have a uniform distribution of 10 periodic ripples. The surface quality of the workpiece is linearly detected for Figure 19(a). A line is drawn from the extension to the center on the test surface topography. The detected line segment is shown in Figure 20(a), and the detection result of the line segment is shown in Figure 20(a), and the detection result of the line segment is shown in Figure 20(b). It can be seen that the curve value from edge to center is also linearly reduced, the slope of the line segment is also negative, and a concave profile is shown in the workpiece center, which is similar to Figure18.

The turning rotation speed is set to 1000r/min, and set to the reverse rotation. The workpiece is machined from the opposite feed direction. The

turning process is shown in Figure 16 (b). In order to eliminate some external interference, the same workpiece surface is machined, reciprocating machining many times. The machined results are shown in Figure21. It can be seen from Figure 21 (b) that the surface quality is poor and the workpiece surface topography has also drawn from the extension to the center on the tested surface topography. The detected line segment is shown in Figure 22 (a). Figure 22(b) shows the detection result of the line segment, and it can be seen that the detected value from edge to center almost increases linearly. The slope of the line segment is positive and the workpiece center has a convex shape, which is different to Figures 18 and 20. In order to further verify the circumferential vibration frequency of the workpiece surface irrelevant with the turning rotation speed, another rotation speed is set to n=900r/min, the feed rate is f=9μm/rev, and the experimental result is shown in Figure 23. There are also 10 cycles of circumferential ripples in Figure 23. Compared to the tested results, the circumferential vibration frequency of the star pattern in the workpiece surface is the same value with different speeds, which has 10 cycle ripples in the circumferential direction.

To eliminate the influence of the three-jaw chuck on the surface topography, another machining experiment using a vacuum chuck to fix the workpiece (5A06) is carried out. The turning speed is set to 1200r/min, the feed speed is 10μm/ rev, and other parameters are unchanged. The turning process and machined workpiece are shown in Figure 24. The tested results of the machined surface are shown in Figure 25 and 26. It can be seen from the figure that there are 10 ripples on the surface topography, which can effectively eliminate the influence of the three-jaw chuck on the workpiece. Compared to machined workpiece surfaces, the machined surfaces have the same profile under different speeds, that is, cyclical ripple. Although the amplitude values are different, the vibration frequency is more consistent. It can be noted that the vibration cycle is derived from the spindle system, and the vibration frequency is independent of the spindle speed.

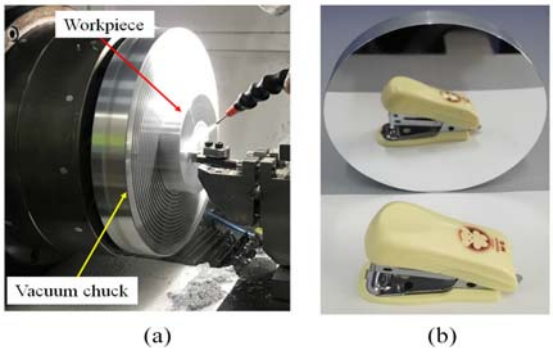

Figure 24. Tested result of the machined surface (n=1200r/min):(a) Turning process fixed on a vacuum chuck; (b) Machined workpiece.

After the above analysis, although there are some different amplitudes of the surface topography betweenthe experimental results and the simulation results, which are related to other external disturbances such as spindle misalignment and motor axial offset, the overall trend of the surface topography are similar to the simulation, which is also a guide line on how to check for motor imperfection. Therefore, to gain the high quality of the workpiece surface, the influence of UMF should be considered before design and installation of the spindle system.

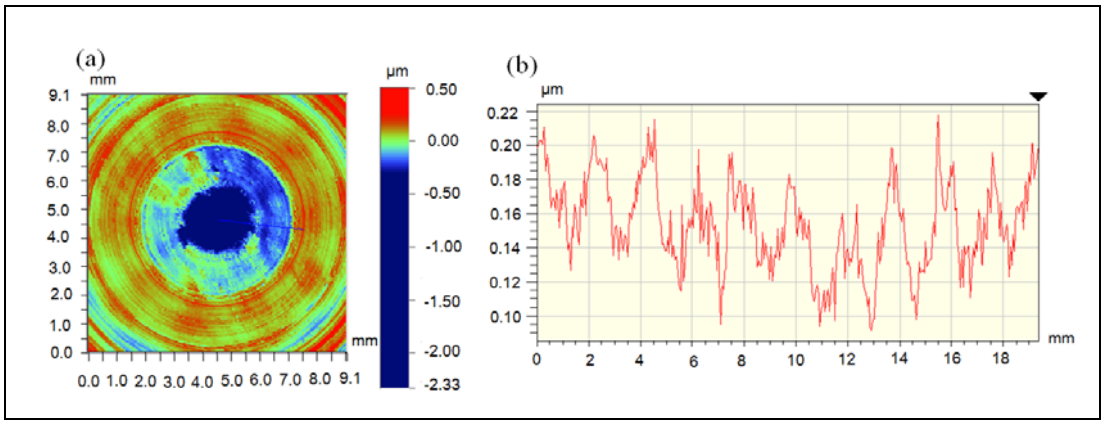

Figure 25. Tested result of a circle on the machined surface (n=1200r/min): (a) position of an extracted circle curve. (b) value change of the curve.

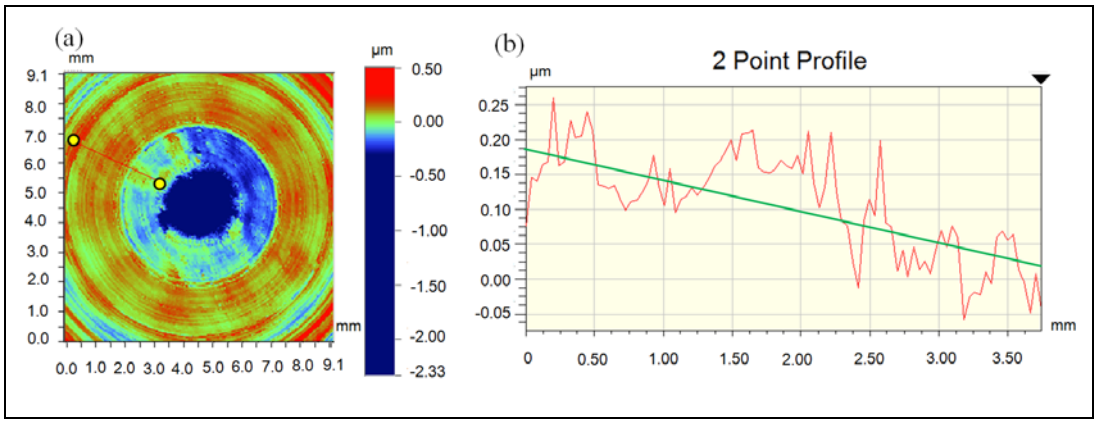

Figure 26. Tested result of a line segment on the machined surface under forward turning (*n*=1200r/min): (a) position of a line, (b) value change of the curve.

Conclusions

A theoretical prediction and experimental verification for researching the periodic UMF in an ABMS is presented in this article. The dynamic characteristics of the UMF on ABMS and its effects on machining have been discussed in detail. It has been shown that the UMF affects surface topography. Based on the analysis and experimental results, the following conclusions can be summarized:

1. A 10/12 (10 poles and 12 slots) motor with MRE is analyzed at unload and load conditions, respectively. It is verified that the number of poles and slots has an influence on the periodic fluctuation of UMF. Meanwhile, the periodic fluctuation of the spindle caused by UMF changes the turning depth in the *Z* direction.
2. The MRE has significant influence of the surface generation. A 10-cycle-per-revolution pattern has been found in the machined surface, which is consistent with vibratons of UMF.
3. The prediction of the forming profile generation in end face turning is achieved on the basis of the proposed model. It is found that the angle between the direction of the UMF and the feed direction has a certain relationship to the

wprkpiece surface shape, which can effectively predict the eccentric direction of the motor.

Declaration of conflicting interests

The author(s) declared no potential conflicts of interest with respect to the research, authorship and/or publication of this article.

Funding

The authors gratefully acknowledge financial support of the International Science & Technology Cooperation Program of China (No. 2015DFA70630), the National Natural Science Foundation of China (Grant Nos.51505107 and 51705462), Zhejiang Provincial Natural Science Foundation of China (LQ16E050012), and China Scholarship Council (CSC).

References

1. Ashok S D, Samuel G L. Modeling, measurement, and evaluation of spindle radial errors in a miniaturized machine tool. Int. J. Adv. Manuf. Technol 2012; 59(5):445-461.
2. Tauhiduzzaman M, Yip A, Veldhuis S C. Form error in diamond turning. Precis. Eng 2015; 42: 22-36.
3. Liu X, Zhang X, Fang F, et al. Identification and compensation of main machining errors on surface form accuracy in ultra-precision diamond turning. Int. J. Mach. Tools 2016, 105:45-57.
4. Li Y T, Fan K C. A novel method of angular positioning error analysis of rotary stages based on the Abbe principle[J]. Proc IMechE, Part B: J Engineering Manufacture 2017, DOI: 10.1177/0954405416688936.
5. Chen D, Gao X, Dong L, et al. An evaluation system for surface waviness generated by the dynamic behavior of a hydrostatic spindle in ultra-precision machining. Int J Adv Manuf Technol 2017, 91(5-8):2185-2192.
6. Zhang S J, To S. Spindle vibration influencing form error in ultra-precision diamond machining. P I Mech Eng C-J Mec 2016; 1989-1996: 203-210.
7. Deng C, An C, Wei B, et al. Investigation on the influence of aerostatic pressure upon surface generation in flycutting. Proc IMechE, Part B: J Engineering Manufacture 2018; DOI: 10.1177/0954405418780164.
8. Ebrahimi R, Ghayour M, Khanlo H M. Nonlinear dynamic analysis and experimental verification of a magnetically supported flexible rotor system with auxiliary bearings. Mech Mach Theory, 2018, 121:545-562.
9. Lee C, Seol H S, Lee J Y, et al. Optimization of Vibration Noise Characteristics of Skewed Permanent Brushless Direct Current Motor. IEEE T Magn 2017; PP(99) : 1-1.
10. Sung S J, Jang G H, Jang J W, et al. Vibration and Noise in a HDD Spindle Motor Arising from the Axial UMF Ripple. IEEE T Magn 2013; 49(6): 2489-2494.
11. Kim D J, Kim H J, Hong J P, et al. Estimation of Acoustic Noise and Vibration in an Induction Machine Considering Rotor Eccentricity. IEEE T Magn 2014; 50(50): 857-860.
12. Song JY, Kang, KJ, Kang, CH, et al Cogging torque and unbalanced magnetic pull due to simultaneous existence of dynamic and static eccentricities and uneven magnetization in permanent magnet motors, IEEE T Magn 2017; 53(3): 8200609.
13. Han X and Palazzolo A. Unstable force analysis for induction motor eccentricity. J Sound Vib 2016; 370:230-258.
14. Qiao X and Hu G. The investigation of unbalanced vibration in flexible motorized spindle-rotor system. Mach Sci Technol 2016; 20(3): 425-439.
15. Wang J, Jing M, Fan H, et al, Study on unbalance magnetic pull of the motorized spindle under different rotor eccentricities. In: International Conference on ubiquitous robots and ambient intellidence, Xi'an, China, 19-22 August 2016, pp.781-785. New York: IEEE.
16. Kim J Y, Sung S J, Jang G H. Characterization and Experimental Verification of the Axial Unbalanced Magnetic Force in Brushless DC Motors. IEEE T Magn 2012; 48(11) : 3001-3004.
17. Chen X, Liu J, He Y, et al. An integrated model for high-speed motorized spindles - Dynamic behaviors. P I Mech Eng C-J Mec 2013; 227(11): 2467-2478.
18. Zhang S J, To S, Cheung C F, et al., Dynamic characteristics of an aerostatic bearing spindle and its influence on surface topography in ultra-precision diamond turning. Int J Mach Tool Manuf 2013; 62(1):

1-12.

19. Liang Y, Chen W, Bai Q, et al., Design and dynamic optimization of an ultraprecision diamond flycutting machine tool for large KDP crystal machining. Int J Adv Manuf Technol 2013; 69(1-4): 237-244.
20. Chen G, Sun Y, Zhang F, et al., Influence of ultra-precision flycutting spindle error on surface frequency domain error formation. Int J Adv Manuf Technol 2017; 88(9); 3233-3241.
21. Chen G, Sun Y, An C, et al. Measurement and analysis for frequency domain error of ultra-precision spindle in a flycutting machine tool. P I Mech Eng B-J Eng 2016; DOI: 10.1177/0954405416673102.
22. Jin L, Yan Z, Xie L, et al. An experimental investigation of spindle rotary error on high-speed machining center. Int. J. Adv. Manuf. Technol 2014; 70(1); 327-334.
23. Zhang P, Chen X. Thermal-mechanical coupling model-based dynamical properties analysis of a motorized spindle system. Proc IMechE, Part B: J Engineering Manufacture 2016; 230(4): 732–743.
24. Liu J, Chen X. Dynamic design for motorized spindles based on an integrated model. Int. J. Adv. Manuf. Technol 2014; 71(9);1961-1974.
25. Kang C, Kang K, Song J, et al. Axial Unbalanced Magnetic Force in a Permanent Magnet Motor due to a Skewed Magnet and Rotor Eccentricities. IEEE T Magn 2017; PP(99) : 1-1.
26. Kim, D, Noh MD and Park YW. Unbalanced magnetic forces due to rotor eccentricity in a toroidally wound BLDCmotor. IEEE T Magn 2016; 52(7): 8203204.
27. Ma, J, Zhu ZQ and Wu L. Influence of slot/pole combination and magnet thickness on unbalanced magnetic force in PM machines with different rotor eccentricities and magnetizations. In: International conference on electrical machines and systems (ICEMS), Sydney, NSW, Australia, 11-14 August 2017. New York: IEEE.
28. Xia ZP, Zhu ZQ, Wu LJ, ET AL. Comparison of radial vibration forces in 10-pole/12-slot fractional slot surface-mounted and interior PM brushes AC machines. In: International conference on electrical machines, Rome, 6-8 September 2010, New York: IEEE.
29. Usman I. Rotary-axial spindle design for large load precision machining applications. Vancouver, BC, Canada: The University of British Columbia, 2010.
30. Zhang SJ, Yu JJ, To S, et al. A theoretical and experimental study of spindle imbalance induced forced vibration and its effect on surface generation in diamond turning, Int J Mech Tool Manu 2018; 133: 61-71.
31. Wu Q, Sun Y, Chen W, et al. Effect of motor rotor eccentricity on aerostatic spindle vibration in machining processes. Proc IMechE, Part C: J Mechanical Engineering Science 2018; 232(7): 1331-1342.
32. Chen G, Liang Y and Sun Y. Frequency domain error analysis in turning. Int J Adv Manuf Tech 2014; 73 (5-8): 929-940.
33. He CL, Zong WJ and Zhang JJ. Influencing factors and theoretical modeling methods of surface roughness in turning process: state-of-the art. Int J Mech Tool Manu 2018; 129:15-26.
34. Chen W, Lu L, Yang K, et al. A novel machine tool design approach nased on surface generation simulationand its implementation on a fly cutting machine tool. Int J Adv Manuf Tech 2015; 80(5-8): 829-837.
35. Valavi M, Nysveen A, Nilssen R, et al. Influence of Pole and Slot Combinations on Magnetic Forces and Vibration in Low-Speed PM Wind Generators. IEEE T Magn 2014;50(5); 1-11.
36. Rezig A, Mekideche M R, Djerdir A. Effect of Rotor Eccentricity Faults on Noise Generation in Permanent Magnet Synchronous Motors. Prog In Electromagn Res 2010; 87(15) :117-132.
37. Dorrell D G. Sources and Characteristics of Unbalanced Magnetic Pull in Three-Phase Cage Induction Motors With Axial-Varying Rotor Eccentricity. IEEE T Ind Appl 2011; 47(1) : 12-24.
38. Faiz J, Ebrahimi B M, Toliyat H A. Effect of Magnetic Saturation on Static and Mixed Eccentricity Fault Diagnosis in Induction Motor. IEEE T Magn 2009;45(8); 3137-3144.
39. Yu Y, Bi C, Hla P N, et al. Incline Unbalanced Magnetic Pull Induced by Misalignment Rotor in PMSM. IEEE T Magn 2013; 49(6); 2709-2714.
40. Kawase Y, Yamaguchi T, Sano S, et al. Effects of off-center of rotor on distributions of electromagnetic force. IEEE T Magn 2005; 41(5); 1944-1947.

41. Kim J H, Lee S K. Micro-patterning technique using a rotating cutting tool controlled by an electromagnetic actuator. Int. J. Mach. Tools 2016; 101: 52-64.

Appendix I

Notation

B_r Radial air-gap flux density

B_θ Tangential air-gap flux density

f_r Radial force density

f_θ Tangential force density

F_0 Axial component force

F Unbalanced magnetic force

k Slope of a rotor tilt

l_1 Distance between the position of UMF to air inlet position of the left radial support

l_2+l_3 Distance between two rows of radial air inlets

l_4 Distance between a position of the right radial air inlet and surface of the workpiece

l_5 Diameter of axial air inlets (mm)

r Distance between a machining point to a workpiece center

R Distance between a centroid and a machining point

γ Torsion angle formed by two lines

η Angle between a line and a vertical direction

θ Angular position of rotor with reference to an axis of a magnetic pole

μ_0 Permeability of air